HHS Public Access

Author manuscript

Solid State Nucl Magn Reson. Author manuscript; available in PMC 2022 February 01.

Published in final edited form as:

Solid State Nucl Magn Reson. 2021 February ; 111: 101710. doi:10.1016/j.ssnmr.2020.101710.

Recent developments in deuterium solid-state NMR for the detection of slow motions in proteins

Liliya Vugmeyster*

Department of Chemistry, University of Colorado Denver, Denver CO USA 80204

Abstract

Slow timescale dynamics in proteins are essential for a variety of biological functions spanning ligand binding, enzymatic catalysis, protein folding and misfolding regulations, as well as protein–protein and protein–nucleic acid interactions. In this review, we focus on the experimental and theoretical developments of ^{2}H static NMR methods applicable for studies of microsecond to millisecond motional modes in proteins, particularly rotating frame relaxation dispersion ($R_{1\rho}$), quadrupolar Carr–Purcell–Meiboom–Gill (QCPMG) relaxation dispersion, and quadrupolar chemical exchange saturation transfer NMR experiments (Q-CEST). With applications chosen from amyloid-β fibrils, we show the complementarity of these approaches for elucidating the complexities of conformational ensembles in disordered domains in the non-crystalline solid state, with the employment of selective deuterium labels. Combined with recent advances in relaxation dispersion backbone measurements for ^{15}N/^{13}C/^{1}H nuclei, these techniques provide powerful tools for studies of biologically relevant timescale dynamics in disordered domains in the solid state.

Graphical Abstract

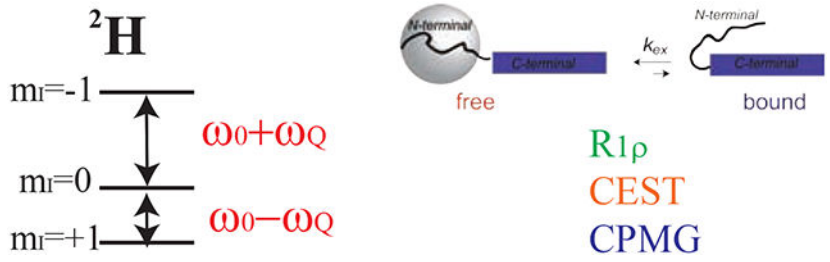

Keywords

deuterium NMR; solid-state NMR; protein dynamics; relaxation dispersion

*To whom correspondence should be addressed: LILIYA.VUGMEYSTER@UCDENVER.EDU.

Declaration of interests

The authors declare that they have no known competing financial interests or personal relationships that could have appeared to influence the work reported in this paper.

1. Introduction

Dynamical modes in proteins are essential for a variety of biological functions spanning ligand binding, enzymatic catalysis, protein folding and misfolding regulations, as well as protein–protein and protein–nucleic acid interactions.[1,2,3,4] Slow motions in microseconds and milliseconds are recognized as the most important of these regulations and a variety of methods have been developed to probe them, in which solution and solid-state NMR techniques play a central role.[5] The solid phase allows the direct observation of timescales of the order of or larger than the typical overall molecular tumbling times found for globular proteins in solution and also permits for the investigation of the hydration dependence of the dynamics.[6,7,8] For non-soluble proteins such as those found in membranes and misfolded fibrillar aggregates, solid-state techniques are of particular importance.[9,10,11,12]

Recent advances in solid-state NMR techniques for the characterization of microsecond–millisecond range dynamics have focused on relaxation dispersion-based approaches probing the backbone ^{1}H, ^{13}C, and ^{15}N sites with site resolution enabled by magic-angle spinning (MAS).[9,13,14,15,16,17,18,19,20,21,22,23,24,25,26,27,28] In particular, much effort has been devoted to Carr–Purcell–Meiboom–Gill (CPMG)-based and rotating frame relaxation techniques ($R_{1\rho}$), both of which can probe the fluctuations of either the isotropic chemical shift or the reorientations of the dipolar and chemical shift anisotropy tensors. The isotropic component is often analyzed within the Bloch–McConnell formalism[29] in analogy with solution NMR approaches,[30] while the fluctuations of the anisotropic tensors often require the full Liouvillian treatment. The near-rotary Resonance Relaxation Dispersion technique is an example of one of these recently developed techniques for anisotropic interactions.[13,16,18,23]

Spin-1 deuterium nuclei are known to be sensitive dynamic probes and they represent a convenient system from theoretical and experimental standpoints: the major interaction is quadrupolar coupling with tensors in the 150–200 kHz range.[6,7,31,32] The resulting spectrum is narrower than for other commonly considered quadrupolar nuclei. Compared with the magnitude of the quadrupole interaction, the CSA and dipolar interactions for the ^{1}H, ^{13}C, and ^{15}N nuclei can be neglected in most cases. The resulting theoretical and computational treatments thus essentially represent a single particle case. Deuteron NMR in the solid state can be particularly advantageous for studies of motions in protein side-chains.[7]

This review summarizes recent developments in ^{2}H solid-state NMR techniques for applications to investigations of slow motions in proteins with examples chosen primarily for the insoluble amyloid fibrils of amyloid-β (Aβ) protein implicated in Alzheimer's disease. The primary focuses are the $R_{1\rho}$, quadrupolar chemical exchange saturation transfer (Q-CEST), and time-domain quadrupolar CPMG (QCPMG) techniques (Figure 1), which we describe in detail for static conditions and discuss the future outlook for coupling them with the MAS approach. More traditional line-shape analysis techniques have been widely employed since the 1970s and provide the groundwork for all other approaches. They have been extensively reviewed elsewhere[6,7,12,31,32,33] and we often compare the dynamical

ranges of our techniques with those possible with line-shape analysis. They encompass a wide range of applications including globular proteins, peptides absorbed on surfaces, membrane proteins, and amyloid fibrils.[8,33,34,35,36,37,38] Of particular note is the alternative modeling approach proposed by Meirovitch and coworkers.[39]

2. Theory

The basis of the following operators constitutes the density matrix for the spin 1 system:[44]

$$\hat{S}_x = \frac{1}{2}\begin{pmatrix}0&1&0\\1&0&1\\0&1&0\end{pmatrix}, \hat{S}_y = \frac{1}{2}\begin{pmatrix}0&-i&0\\i&0&-i\\0&i&0\end{pmatrix}, \hat{J}_x = \frac{1}{2}\begin{pmatrix}0&-i&0\\i&0&i\\0&-i&0\end{pmatrix}, \hat{J}_y = \frac{1}{2}\begin{pmatrix}0&1&0\\1&0&-1\\0&-1&0\end{pmatrix}$$
$$\hat{J}_z = \frac{1}{\sqrt{2}}\begin{pmatrix}0&0&-i\\0&0&0\\i&0&0\end{pmatrix}, \hat{K} = \frac{1}{\sqrt{2}}\begin{pmatrix}0&0&1\\0&0&0\\1&0&0\end{pmatrix}, \hat{S}_z = \frac{1}{\sqrt{2}}\begin{pmatrix}1&0&0\\0&0&0\\0&0&-1\end{pmatrix}, \hat{Q} = \frac{1}{\sqrt{6}}\begin{pmatrix}1&0&0\\0&-2&0\\0&0&1\end{pmatrix}, . \quad (1)$$

The first row represents the single-quantum coherences, followed by two double-quantum coherences, $\hat{K}$ and $\hat{J}_z$. $\hat{S}_z$ and $\hat{Q}$ stand for the Zeeman and quadrupolar order.

During the spin-locking or saturation periods and in the frame rotating with the Larmor frequency, the secular part of the Hamiltonian is given by

$$\hat{H} = \sqrt{\frac{2}{3}}\omega_Q\hat{Q} + \sqrt{2}\omega_{RF}(\hat{S}_x\cos\Omega t + \hat{S}_y\sin\Omega t),$$

where ω_{RF} is the RF field strength and Ω is its off-resonance offset.

$$\omega_Q = \frac{3\pi}{2}C_q\left(\frac{3\cos^2\theta - 1}{2} + \frac{\eta}{2}\sin^2\theta\cos 2\phi\right) \quad (2)$$

is the frequency of the secular part of the quadrupole interaction. The quadrupolar coupling constant and the asymmetry of the tensor are $C_q = \frac{eQq_{zz}}{h}$, and $\eta = \frac{q_{xx} - q_{yy}}{q_{zz}}$, respectively. eQ is the electric quadrupole moment of the nucleus and $|q_{zz}| \geq |q_{yy}| \geq |q_{xx}|$ are the components of the electric field gradient tensor in the principal axes system. η is defined in the interval $0 \leq \eta \leq 1$. The typical values of ^{2}H quadrupolar coupling constants are in the 150 to 200 kHz range. The relative orientation of the principal axis system of the quadrupole interaction and the laboratory frame is given by the angles (θ, ϕ).

The value of ω_Q for an individual crystallite fluctuates in the presence of molecular motions as a result of alterations in the principal axis system's orientation. The terms fluctuating with single and double Larmor frequencies are also part of the Hamiltonian and are treated within the Redfield theory formalism (for details see Eq. 27-34 in reference[31]).

The secular part of the Hamiltonian in the frame additionally rotating with the offset frequency Ω is given by:

$$\widehat{H}_{sec} = \sqrt{\frac{2}{3}}\omega_Q \widehat{Q} + \sqrt{2}\omega_{RF}\hat{S}_x + \sqrt{2}\Omega\hat{S}_z \tag{4}$$

The evolution of spin system is written in the Liouville-von-Neumann framework when the dynamics is taken into account. Specifically, the motions can be taken into account through discrete jumps between several sites representing different internal molecular configurations. Continuous motions can be reasonably represented by a series of closely spaced sites. Whether slow time scales can be adequately described by the Redfield approximation depends on the exact nature of molecular motion. As we argue below, the approximation must be replaced by more exact treatment for large scale fluctuations. In contrast, the rapidly oscillating terms of the non-secular Hamiltonian, which do not appear in Eqs. (3) and (4), are treated in the second order of the perturbation theory within the Redfield formalism.[45]

The evolution equation in the presence of discrete conformational jumps between n sites with the different values of ω_Q is given by

$$\frac{d}{dt}\begin{pmatrix}\rho_1\\ \rho_2\\ \vdots\\ \rho_n\end{pmatrix} = \begin{pmatrix} A_1 + K_{11} & K_{12} & \cdots & K_{1n} \\ K_{21} & A_2 + K_{22} & \cdots & K_{2n} \\ \vdots & \vdots & \ddots & \vdots \\ K_{n1} & K_{n2} & \cdots & A_n + K_{nn}\end{pmatrix}\begin{pmatrix}\rho_1\\ \rho_2\\ \vdots\\ \rho_n\end{pmatrix} \tag{5}$$

where $\rho_i = (S_x, S_y, J_x, J_y, J_z, K, S_z, Q)^T$ are the components of the density matrix for a site i in the basis of the operators of Eq. (1). For the on-resonance situation, this reduces to the 4×4 space with $\rho_i = (S_x, J_x, K, Q)^T$. The other four components of the density matrix are decoupled and do not have to be taken into account. The CEST and $R_{1\rho}$ experiments also differ in the initial conditions for solving Eq. (5), which are $\rho_i(0) = w_i(0,0,0,0,0,0,1,0)^T$ for the CEST experiment and $\rho_i(0) = w_i(1,0,0,0,0,0,0,0)^T$ for the $R_{1\rho}$ experiment, where w_i is the relative weight (occupation number) of site i.

The conformational exchange enters via the off-diagonal elements $K_{ij} = k_{ij}I$, where I is the 8×8 identity matrix. The diagonal terms include the superoperator of coherent evolution as well as relaxation terms due to the rapidly oscillating contributions. The full 8×8 evolution A_i matrices is then:

$$A = \begin{pmatrix} -r_1 & -\Omega & -\omega_Q & 0 & 0 & 0 & 0 & 0 \\ \Omega & -r_1 & 0 & \omega_Q & 0 & 0 & -\omega_{RF} & 0 \\ \omega_Q & 0 & -r_2 & \Omega & 0 & -\omega_{RF} & 0 & -\sqrt{3}\omega_{RF} \\ 0 & -\omega_Q & -\Omega & -r_2 & \omega_{RF} & 0 & 0 & 0 \\ 0 & 0 & 0 & -\omega_{RF} & -r_3 & 2\Omega & 0 & 0 \\ 0 & 0 & \omega_{RF} & 0 & -2\Omega & -r_3 & 0 & 0 \\ 0 & \omega_{RF} & 0 & 0 & 0 & 0 & -r_4 & 0 \\ 0 & 0 & \sqrt{3}\omega_{RF} & 0 & 0 & 0 & 0 & -r_5 \end{pmatrix} \tag{6}$$

The secular contributions of the rapidly oscillating terms (with the frequencies of ω_L and $2\omega_L$) are calculated to be: [46]

$$r_1 = \frac{5}{2}J_1(\omega_L) + J_2(2\omega_L)$$

$$r_2 = \frac{1}{2}J_1(\omega_L) + J_2(2\omega_L)$$

$$r_3 = J_1(\omega_L) + J_2(2\omega_L)$$

$$r_4 = J_1(\omega_L) + 4J_2(2\omega_L)$$

$$r_5 = 3J_1(\omega_L)$$

The relaxation due to changes in ω_Q arises directly from the solution of Eq. (5). In the Redfield limit, these terms would give rise to J_0. The static magnetic field strength dependence enters Eqs. (5) and (6) solely through the relaxation terms r_1 to r_5, which are only sensitive to timescales of the order of ω_L. Thus, for slow timescale motions, the main contribution to relaxation is expected to be field independent.

For the Redfield limit to hold, the relaxation rate needs to be smaller than the rate of the motions that cause it.[45] In particular, the transitions involving different Zeeman levels yield a rate of the order of $\frac{\omega_Q^2 k}{\omega_L^2 + k^2} < \left(\frac{\omega_Q}{\omega_L}\right)^2 k \ll k$, where k stands for the motional rate constant. If the Redfield approximation were used to calculate the relaxation rates due to changes in ω_Q, their value would be estimated as $r_Q \sim \frac{\omega_Q^2}{k}$. This condition serves as an upper limit for the relaxation rate because the change in ω_Q is taken as the value of ω_Q itself. When $r_Q \ll k$ holds, the Redfield limit is applicable. The sufficient condition can be written as $\omega_Q \ll k$. The Redfield limit is also an adequate approximation if the changes in ω_Q are much smaller than ω_Q itself (e.g., the case of small-angle fluctuations) even for the case of slow motions. The Redfield and Liouvillian approaches were recently compared for ^{1}H $R_{1\rho}$ relaxation under MAS conditions.[22] Further, the Redfield treatment is adequate for small-angle fluctuations and spinning speeds far from the rotary resonance conditions, while the Liouvillian treatment is necessary for other cases.

For the case of the QCPMG experiment, no spin-locking field is involved and thus the only secular term in the Hamiltonian is $\sqrt{\frac{2}{3}}\omega_Q\hat{Q}$. Thus, there is no mixing of the single-quantum

coherences of Eq. (1) during the evolution period and only the $\hat{S}_x$ coherence needs to be taken into account.

To gain a qualitative insight into the behavior of the coherent (oscillating) and non-coherent contributions to the relaxation, we focus on the on-resonance $R_{1\rho}$ experiment. This case leads to the space of four inter-converting coherences (S_x, J_x, K, Q). We first consider the limit of the coherent contributions in the absence of motions:

$$\frac{d}{dt}\begin{pmatrix} S_x \\ J_x \\ K \\ Q \end{pmatrix} = \begin{pmatrix} 0 & -\omega_Q & 0 & 0 \\ \omega_Q & 0 & -\omega_{RF} & -\sqrt{3}\omega_{RF} \\ 0 & \omega_{RF} & 0 & 0 \\ 0 & \sqrt{3}\omega_{RF} & 0 & 0 \end{pmatrix}\begin{pmatrix} S_x \\ J_x \\ K \\ Q \end{pmatrix} \tag{7}$$

The eigenvectors of Eq. (7) with the corresponding eigenvalues are given by[46]

$$\begin{aligned} &\frac{2\omega_{RF}}{\omega_1}\hat{S}_x + \frac{\omega_Q}{2\omega_1}(\hat{K} + \sqrt{3}\hat{Q}), 0 \\ &\frac{\sqrt{3}}{2}\hat{K} - \frac{1}{2}\hat{Q}, 0 \\ &\frac{\omega_Q}{\sqrt{2}\omega_1}\hat{S}_x \pm \frac{i}{\sqrt{2}}\hat{J}_x - \frac{\omega_{RF}}{\sqrt{2}\omega_1}\left(\hat{K} + \sqrt{3}\hat{Q}\right), \pm i\omega_1 \end{aligned} \tag{8}$$

where $\omega_1^2 = \omega_Q^2 + 4\omega_{RF}^2$. The frequency ω_1 depends on the crystallite orientations. Motions modulate the values of ω_Q, but an additional variability arises due to the inhomogeneity of the RF field. Thus, for the third and fourth eigenvectors, the complexity of the oscillations depends on multiple factors other than the relaxation. The initial decay of magnetization has a strong oscillating component, leading to effective "dead-time," which has to be excluded from the analysis [41]. Similar dead-time considerations have to be applied to the analysis of ^{15}N $R_{1\rho}$ relaxation under MAS conditions.[23] By contrast, the first two eigenvectors, $\frac{2\omega_{RF}}{\omega_1}\hat{S}_x + \frac{\omega_Q}{2\omega_1}\left(\hat{K} + \sqrt{3}\hat{Q}\right)$ and $\frac{\sqrt{3}}{2}\hat{K} - \frac{1}{2}\hat{Q}$, are non-oscillating eigenvectors. The term $\frac{2\omega_{RF}}{\omega_1}\hat{S}_x + \frac{\omega_Q}{2\omega_1}\left(\hat{K} + \sqrt{3}\hat{Q}\right)$ governs the magnetization decay curves beyond the dead-time for the on-resonance single quantum $R_{1\rho}$ measurement. This indicates that relatively strong RF fields are needed for the effective locking and detection of $\hat{S}_x$ magnetization. The analysis points to an option to focus instead on the quadrupolar order coherence $\hat{Q}$, for which the effectiveness of locking is best for smaller RF fields. This option is discussed further in the Future Directions section.

3. Experimental approaches

3.1 Hardware

The optimal performance of the console and probe setup for the ^{2}H static measurements in Figure 1 is governed by three major factors: the power requirements of the 2–2.5 μs 90° pulses needed to cover the full-width powder pattern, the spin-lock/QCPMG train power

duty cycle requirements, and the minimization of the acoustical ring-down to the 20–30 μs range, beyond which the signal loss due to transverse relaxation becomes pronounced for protein samples. The inhomogeneity of the coil is another consideration, as it leads to dampening of the observed coherent oscillations. To accommodate a wide range of temperatures, the setup needs to be optimized to protect the magnet from cold or hot air by adjusting frame cooling flows and adding a flow line directly into the bore of the magnet.

3.2 Sample Preparation

Sample preparation for ^{2}H static NMR often requires introduction of site-specific labels to obtain residue-specific data. For small peptides up to about 100 residues in length, solid-state peptide synthesis is a viable option. Another route is the usual protein expression methodologies combined with strategies to label selective residue types.[47] For protein powder hydration, water can be incorporated by either vapor diffusion or direct pipetting of regular or deuterium depleted H_2O. A typical required amount of material spans 10 to 30 mg range for proteins with 30 to 70 amino acids.

3.3 Temperature Control

Temperature control is important for the accurate determination of dynamics and avoidance of sample damage or dehydration. Lead nitrate can serve as a useful reference temperature calibration standard, establishing the calibration curve without the additional RF heating component. Temperature calibration can be performed by recording static lead nitrate line shapes[48] and using the freezing point of D_2O, 3.8°C, as the fixed point for the calibration. A lanthanide complex, H_6 TmDOTP, was also recently introduced as a sensitive internal thermometer by Zhang et al.[49] As mentioned earlier, in QCPMG measurements, the number of echoes should be limited to avoid sample heating, in addition to adjusting the length of the inter-scan delay. RF heating in QCPMG experiments usually cannot be judged directly from the temperature or heater power reported by the temperature controller. However, lead nitrate calibration experiments can help in quantifying this effect.[50] For hydrated powder protein samples, we have found that limiting the acquisition to 15–20 echoes with a recycle delay of 0.5–0.8 s is usually sufficient to avoid internal heating.

In the Q-CEST experiment, the RF field is weak (~1–3 kHz) but long saturation times greater than 10 ms require recycle delays of at least 0.8 s for hydrated protein samples. The $R_{1\rho}$ measurement with the RF field strength in the 20–35 kHz range can introduce substantial additional heating of the sample. While the heat compensation block controls for identical heating throughout different delays of the same RF field, different RF fields still need to be controlled for differential heating effects. Samples with sensitive values of T_1 as a function of temperature can be used as standards to calibrate differential relaxation delays for each value of the RF field. As a first approximation, these calibrated values of the inter-scan delays can be used for the protein samples of interest when the same probe is employed.

3.4 Performing the experiment

3.4.1 $R_{1\rho}$ experiment—The pulse sequence of Figure 1B utilizes a heat compensation block to ensure a constant total spin-lock time throughout all relaxation delays and is

conceptually analogous to the pulse sequences presented by Vega for half-integer quadrupolar spins.[44] This pulse sequence has also been employed by Wimperis and coworkers.[51] As with all relaxation dispersion techniques, the key factor to probing the motions is to obtain the relaxation rates as a function of the spin-lock field that renders a different extent of the refocusing of slow motions.[30]The spin-lock field strength can be calibrated using a pulse sequence similar to the one in Figure 1B by adding a nutation pulse with a 90° phase shift after the spin-lock period.

For hydrated protein powders, spin-lock fields higher than 25–35 kHz and relaxation times beyond 20–30 ms can lead to temperature gradients throughout the sample. The lowest field that can maintain the locking of the magnetization depends on the effective quadrupolar coupling constant of individual samples. For methyl groups the typical value of C_q is 53-57 kHz after averaging over fast methyl jumps, leading to the minimum effective locking at around 15 kHz RF field strength.[42] Smaller RF amplitudes in this case will not lock all of the crystallite orientations and, thus, can contribute to changes in the effective relaxation rate which should not be interpreted as a consequence of motions. If there are additional fast motions that lead to further narrowing of the tensor, the condition on the minimum value of the RF at which the effective locking is obtained is relaxed. This was observed to be the case for the A2-CD_3 site in the hydrated $A\beta_{1–40}$ fibrils, for which the additional fast motions, which will be discussed in section 4.1, led to a very significant tensor narrowing (Figure 2B, right panel). The relatively low signal governs how many points can be sampled along the magnetization decay curves: in general, 10–15 relaxation delays are expected to be sufficient with the lowest value in the 100–400 μs range depending on the extent of the coherent oscillations in the initial decays. The static quadrupole echo detection block (τ—90°—τ), in principle, permits for the relaxation anisotropy analysis. In practice, this is difficult to achieve for protein samples due to low sensitivity and, thus, one usually focuses on the major singularities of the spectra. Magnetization decay curves are in general non-exponential and for higher sensitivity samples one can attempt a double exponentional fit (Figure 2). For low sensitivity samples, a single exponential fit is usually performed, with or without the baseline parameters, depending on the data. It is very important that the modeling procedures utilize relaxation delays that are identical to the experimental conditions.

3.4.2 QCPMG time-domain experiment—Historically, this technique has been developed and applied to enhance the sensitivity of quadrupolar nuclei static line shapes and detect motions based on the line shape.[6,50,52] We adapted this technique to measure the transverse relaxation times in singly labeled protein samples using the time-domain approach. Using Bruker neo console technology led to a significant reduction in artifacts in the magnetization decay curves. Multiple full echoes (Figure 1A) refocus the motions as a function of the spacing interval, $\tau_{QCPMG} = \tau_a + 2\tau_1 + 90°/2$. More than about 20 echoes can introduce significant sample heating and this is recommended as an upper limit for protein samples. The lowest value of τ_{QCPMG} is chosen to avoid sample heating and also limited by the acoustic ringing of the console/probe setup. The maximum value of τ_{QCPMG} is limited only by the length of the decay itself. The typical range for τ_{QCPMG} that we found useful is 50 to 350 μs. The total acquisition length for each value of τ_{QCPMG} defines the timescales of

motions to which the experiment is most sensitive and can govern the shape of the relaxation dispersion profiles, as further demonstrated in Section 4.1. Integrated echo intensities (Figure 3) can usually be fitted to a single-exponential function with no offset. As expected from the theory of quadrupolar coupling interactions, the magnetization decay curves in Figure 2,3 as well as the Q-CEST saturation profiles for the A2-CD_3 site presented in Section 4.2 did not change in the presence of proton decoupling power with 70 kHz power.

3.4.3 Q-CEST experiment—Q-CEST exploits the transfer of the saturation of polarization between different conformational states due to the presence of conformational exchange. Although there are some analogies with the solution NMR CEST and DEST approaches,[30,53,54] the situation is more complex due to the anisotropic nature of the quadrupolar interaction and powder pattern dependence. The measurement is repeated for multiple values of the off-resonance offsets (Figure 1C), usually spanning the full range of the effective quadrupolar coupling constant, and utilizes a weak RF field. A 1–3 kHz RF field strength will likely suffice for most applications and this is governed by the condition that the RF field strength should be smaller than the typical value of the difference in ω_Q in the two exchanging states. In order for the isotropic chemical shift fluctuations to potentially contribute toward the Q-CEST profiles they have to be on the order of 8-12 ppm for the saturation field of 1 kHz. The maximum saturation times employed are governed by the restrictions imposed by the longitudinal relaxation competing with the saturation transfer and sample heating considerations. The minimum saturation times are governed by the efficiency of the conformational exchange (i.e., rate constants and populations). The typical ranges of the saturation times for protein samples are expected to lie between 1 and 40 ms. For offsets close to a zero frequency, a larger number of scans is usually necessary. In some cases, it can be sufficient to perform the experiment for a single value of the RF field and a single value of the saturation time; however, in many cases, it will be useful to have at least two different fields and two different saturation times to provide a better set of constraints of the modeled parameters. Because I_z component commutes with the secular part of the quadrupolar operator, spin-locking by weak RF fields is possible. Due to the weak RF field, it is useful to perform field calibrations by employing a D_2O sample using either methods similar to those described for the $R_{1\rho}$ measurements or a simple power calibration based on a 90° pulse width.

Q-CEST significantly expands the sensitivity range compared with line-shape analysis by orders of magnitude, and qualitative insights can be obtained by examining the modeled saturation profiles for a simple 2-site jump scenario (Figure 4). The experimental and simulated plots are usually shown for the ratios of intensities, at times t and $t = 0$, referred to as $I(t)/I(0)$. The most general approach is to integrate $I(t)$ over either the entire powder pattern or the spectral region most sensitive to the line-shape distortions. Coherent oscillations are expected for I_z, and are most pronounced when $\Omega = \pm\omega_Q$ (blue line in Figure 4C). Motions can significantly broaden these profiles, as shown in Figure 4C.

4. Example applications to Amyloid-β fibril systems

In this section, we demonstrate the applications of the ^2H $R_{1\rho}$, Q-CEST, and QCPMG measurements to elucidate the dynamics of the disordered domain of $A\beta_{1\text{-}40}$ fibrils.

[38,40,41,42] Aβ fibrils, hallmarks of Alzheimer's disease, exist in multiple morphological forms, of which we considered the more toxic 3-fold symmetric polymorph.[55] The disordered N-terminal domain (residues 1–16) has been found to be mobile by multiple studies and has been implicated in the aggregation control of Aβ aggregates.[56,57,58,59,60] These techniques permitted for elucidation of details of the conformational ensemble of the domain. We focused on three selectively labeled sites spread throughout the disordered region, A2-CD_3, τ-H6-D_3, and G9-D_2.

Examples of the experimental results are shown in Figure 5, which display plots of the relaxation times $T_{1\rho} = \frac{1}{R_{1\rho}}$ versus spin-lock field strength and T_2 (QCPMG) versus τ_{QCPMG}. For the A2 and H6 sites, the $R_{1\rho}$ data were fitted to a double-exponential function (see also the magnetization decay examples in Figures 2 and 3); for the G9 site, the quality of the data allowed only for a single-exponential fit with a baseline. The QCPMG measurements were taken for τ_{QCPMG} values between 53 and 303 μs. For these measurements, the direction of the dispersion is the opposite that found in solution NMR for cases of probing isotropic interactions. A possible source of this inversion is the anisotropic nature of the quadrupolar interactions coupled with the solid powder system and different lengths of the time-domain acquisition for small and large τ_{QCPMG} values. We modeled this effect by zooming in on individual crystallite orientations (we refer the reader to Figure S2 in [42]). Tollinger et al.[62] also observed this inversion of the dispersion in the simulation for ^{15}N backbone nuclei CPMG measurements under MAS conditions when the main motional mechanism was assumed to be the reorientation of the anisotropic parts of the dipolar ^{15}N-^{1}H and ^{15}N CSA interactions, rather than the isotropic chemical shift interaction.

The combined results of the ^{2}H line-shape analysis[38] in the wide temperature range and the QCPMG and $R_{1\rho}$ data at the physiological temperature[42] led to the model (Figure 6A) in which two mobile "free" states of the N-terminal domain undergo rotational diffusive motions. Hydration induces significant line shape narrowing of the free state (Figure 7A),[38] allowing for the use of the RF field amplitude as low as 5 kHz in the $R_{1\rho}$ relaxation dispersion measurements. The free states participate in the conformational exchange with a single bound state. In the latter, there are no diffusive motions, the freezing of which likely originates from the transient interactions with the structured hydrophobic core or intramolecular interactions. QCPMG and $R_{1\rho}$ measurements complement each other by probing somewhat different time scales of motions. For the case of the A2 residue, the $R_{1\rho}$ measurements are sensitive to the exchange between the bound state and slow diffusion free state (with $D_2 = 3{\cdot}10^6$ rad^2/s, $k_{ex,2} = 2\text{-}3{\cdot}10^4$ s^{-1} using notation of Figure 6A), while the QCPMG relaxation primarily probes the exchange process of the fast diffusion state (with $D_2 = 1{\cdot}10^8$ rad^2/s, $k_{ex,1} = 2\text{-}3{\cdot}10^5$ s^{-1}).[42] The relative populations of the slow and fast diffusion states are 25% and 75% for the A2-CD_3 site, with a relative total fraction of the bound state of 8% in relation to both free states. The relative fraction of the bound state as well as the population of the slow diffusion state increase along the N-terminal sequence.[38]

For the A2-CD_3 site, we also performed the Q-CEST measurements at RF field strengths of 1.3 and 2.5 kHz and at saturation times of 1 and 20 ms (the laboratory frame longitudinal

relaxation at this site is 50 ms).[40] The profiles (Figure 7B) given by the $I(t)/I(0)$ values were obtained by integrating over the entire spectrum, as no spectral distortions were observed from the line shape. Using the model of Figure 6A with the parameters determined from $R_{1\rho}$ and QCPMG, we obtained a satisfactory fit to the Q-CEST profiles. However, the sensitivity of the fit to the model parameters provides an additional insight into the conformational ensemble of the N-terminal domain. In particular, the combined analysis of all experimental data suggests that the conformational ensemble of the N-terminal domain consists of a range of free states characterized by different diffusion coefficients (Figure 6B). Conformational exchange likely occurs with a single bound state.

5. Other selected ^{2}H solid-state NMR techniques for studies of slow motions

In this section, we briefly mention selected additional ^{2}H solid-state NMR techniques used for studies of slow motions. These techniques have been extensively reviewed previously[6,7,33,37,61,62] and the goal here is to draw some parallels with the more recent approaches discussed in this work. Modifying the traditional line-shape analysis used under static conditions involves the analysis of the *spectral* domain of the QCPMG-acquired data.[52] The techniques improve the sensitivity and increase the dynamical range compared with quadrupolar echo pulse sequences. Sensitivity enhancement is also obtained by analyzing the side-band intensities under MAS conditions.[63] The nature of the multiple echo side-band is fundamentally different from the MAS side-bands: the former arises due to refocusing the spin part of the Hamiltonian, while the latter is due to spatial rotation. The analysis of side-band intensities suffers from a lower resolution for each site than static quadrupolar echo measurements. However, it provides site-specific resolution for samples with different groups labeled with deuterium when their chemical shifts are resolved.[63,64] Wimperis and coworkers[65] analyzed the side-band line shapes themselves, as opposed to their intensities, to overcome this drawback. They also extended this method to compare single-quantum with double-quantum line shapes[66] in a two-dimensional experiment, which provides a sensitive test for the presence of the dynamics. An interesting option is to perform MAS line-shape measurements under a slight offset of the magic angle.[67,68] ^{2}H chemical shift resolution is obtained in the ^{2}H DQ dimension, while the quadrupole parameters can be determined from the line shapes patterns reintroduced in the second dimension by the magic-angle offset.

Laboratory frame ^{2}H T_1 relaxation, while sensitive to fast ps-ns timescales, can provide estimates of slower timescales of the conformational exchange occurring during the relaxation period of the inversion recovery/saturation recovery experiments in the presence of multiple conformers or their distributions.[69] Boutis and coworkers also developed two-dimensional T_1-T_2 measurements with applications to water dynamics in elastin and detected timescales as slow as 10 μs.[70]

6. Future directions

In regard to the $R_{1\rho}$ experiments, in addition to single-quantum coherence, other coherences can be selected in analogy to half-integer quadrupolar nuclei. For the ^{2}H-detected hydrated

protein sites, coherences that are refocused under lower RF fields can be especially advantageous to avoid RF-induced heating. Quadrupolar order coherence is expected to have smaller extent of incoherence oscillation and better refocusing under lower RF field conditions than single-quantum coherence based on the first eigenvector of Eq. (8).[71] The excitation scheme developed by Wimperis and coworkers can be used for the broad-band excitation of the quadrupolar order.[72,73]

An obvious extension of the ^{2}H $R_{1\rho}$ and CEST techniques discussed here is the inclusion of MAS for multiple-labeled samples to achieve site-specific resolution. While this is in principle possible and is a promising direction, a number of challenges have to be overcome. Deuterium itself often does not have sufficient chemical shift resolution. In this case, it can be obtained from the ^{13}C labeled nuclei in the sample, but requires the introduction of polarization transfer steps. Cross-polarization to quadrupole spin 1 nuclei has its own set of challenges and a number of approaches have been developed to optimize the transfer.[74,75,76,77]The efficiency of cross-polarization may be insufficient for dynamic sites such as disordered domains, and INEPT-based transfer approaches can be required in these situations.[78] Special isotopic labeling approaches may also be required to enable optimal site-specific resolutions for complicated systems, such as those used in proton detection schemes.[79] During relaxation blocks, similarly to the cases for ^{13}C and ^{15}N nuclei, rotary resonance conditions have to be taken into consideration when choosing the experimental conditions. An important distinction between these nuclei is that spin 1 leads to major rotary resonances with the RF field not only around an integer multiple of spinning frequency but also at the half-integer spinning frequency, which for spin 1/2 nuclei is seen only for the case of homonuclear interactions.[13,18,19,20,23] Another important difference is the magnitude of the quadrupolar interaction, which is of an order of magnitude larger than those entering two-spin or multiple-spin ½ systems for ^{13}C, ^{15}N, and ^{1}H nuclei. Thus, even for the case of methyl groups with a motionally narrowed tensor due to methyl rotation, spinning speeds beyond 60 kHz are required to average the interactions. For the Q-CEST experiment, the fast/ultrafast MAS conditions could be especially advantageous to avoid breaking the saturation profiles (such as those in Figure 7) into the multiple rotary resonances expected for low-speed MAS.

7. Concluding remarks

Newly adapted ^{2}H solid-state NMR relaxation dispersion and CEST approaches in combination with more traditional line-shape analysis measurements demonstrate great potential for the elucidation of the slow-timescale dynamics of the disordered region of non-crystalline aggregates and fibrils. At present they have been fully explored under static conditions requiring single-site labeling, but there is a clear possibility for extension to MAS conditions. In combination with recent advances in backbone-based $^{15}N/^{13}C$ relaxation dispersion techniques under MAS conditions,[13] this array of tools would constitute a powerful combination for protein dynamics studies of biologically relevant timescales.

Acknowledgements

This work was supported by the National Institutes of Health Grant 1R15-GM111681.

References

[1]. Frauenfelder H, Chen G, Berendzen J, Fenimore PW, Jansson H, McMahon BH, Stroe IR, Swenson J, and Young RD, Proc. Natl. Acad. Sci. U. S. A 106 (2009) 5129–5134. [PubMed: 19251640]

[2]. Berlow RB, Dyson HJ, and Wright PE, J. Mol. Biol 430 (2018) 2309–2320. [PubMed: 29634920]

[3]. Dyson HJ, and Wright PE, Elucidation of the protein folding landscape by NMR in: James T, (Ed.), Nuclear Magnetic Resonance of Biological Macromolecules, Part C, 2005, pp. 299.

[4]. Boehr DD, Nussinov R, and Wright PE, Nat. Chem. Biol 5 (2009) 789–796. [PubMed: 19841628]

[5]. Palmer AG, and Koss H, Chapter Six - Chemical Exchange in: Wand AJ, (Ed.), Methods in Enzymology, Academic Press, 2019, pp. 177–236.

[6]. Vugmeyster L, and Ostrovsky D, Methods 148 (2018) 136–145. [PubMed: 29705208]

[7]. Vugmeyster L, and Ostrovsky D, Prog. Nucl. Magn. Reson. Spec 101 (2017) 1–17.

[8]. Vugmeyster L, Ostrovsky D, Khadjinova A, Ellden J, Hoatson GL, and Vold RL, Biochemistry 50 (2011) 10637–10646. [PubMed: 22085262]

[9]. Linser R, Sarkar R, Krushelnitzky A, Mainz A, and Reif B, J. Biomol. NMR 59 (2014) 1–14. [PubMed: 24595988]

[10]. Krushelnitsky A, and Reichert D, Prog. Nucl. Magn. Reson. Spectrosc 47 (2005) 1–25.

[11]. van der Wel PCA, Solid State Nucl. Magn. Reson 88 (2017) 1–14. [PubMed: 29035839]

[12]. Hong M, Structure 14 (2006) 1731–1740. [PubMed: 17161364]

[13]. Rovó P, Solid State Nucl. Magn. Reson (2020) 101665. [PubMed: 32574905]

[14]. Lakomek N-A, Penzel S, Lends A, Cadalbert R, Ernst M, and Meier B, Chemistry 23 (2017) 9425–9433. [PubMed: 28426169]

[15]. Krushelnitsky A, Zinkevich T, Reif B, and Saalwächter K, J. Magn. Reson 248 (2014) 8–12. [PubMed: 25282442]

[16]. Kurauskas V, Izmailov SA, Rogacheva ON, Hessel A, Ayala I, Woodhouse J, Shilova A, Xue Y, Yuwen T, Coquelle N, Colletier J-P, Skrynnikov NR, and Schanda P, Nature Commun. 8 (2017) 145. [PubMed: 28747759]

[17]. Quinn C, and McDermott A, J. Biomol. NMR 45 (2009) 5–8. [PubMed: 19636799]

[18]. Ma P, Haller JD, Zajakala J, Macek P, Sivertsen AC, Willbold D, Boisbouvier J, and Schanda P, Angew. Chem. (Int Ed.) 53 (2014) 4312–4317.

[19]. Quinn CM, and McDermott AE, J. Biomol. NMR 222 (2012) 1–7.

[20]. Gauto DF, Hessel A, Rovó P, Kurauskas V, Linser R, and Schanda P, Solid State Nucl. Magn. Reson 87 (2017) 86–95. [PubMed: 28438365]

[21]. Rovó P, and Linser R, ChemPhysChem. 19 (2018) 34–39. [PubMed: 29149466]

[22]. Rovó P, and Linser R, J. Phys. Chem. B 121 (2017) 6117–6130. [PubMed: 28534618]

[23]. Krushelnitsky A, Gauto D, Rodriguez Camargo DC, Schanda P, and Saalwachter K, J. Biomol. NMR 71 (2018) 53–67. [PubMed: 29845494]

[24]. Shannon M, Theint T, Mukhopadhyay D, Surewicz K, Surewicz W, Marion D, Schanda P, and Jaroniec CP, ChemPhysChem. 20 (2019) 311–317. [PubMed: 30276945]

[25]. Smith AA, Testori E, Cadalbert R, Meier BH, and Ernst M, J. Biomol. NMR 65 (2016) 171–191. [PubMed: 27423891]

[26]. Schanda P, and Ernst M, Prog. Nucl. Magn. Reson. Spectrosc 96 (2016) 1–46. [PubMed: 27110043]

[27]. Tollinger M, Sivertsen AC, Meier BH, Ernst M, and Schanda P, J. Am. Chem. Soc 134 (2012) 14800–14807. [PubMed: 22908968]

[28]. Keeler EG, Fritzsching KJ, and McDermott AE, J. Magn. Reson 296 (2018) 130–137. [PubMed: 30253322]

[29]. McConnell HM, J. Chem. Phys 28 (1958) 430–431.

[30]. Palmer AG 3rd, J. Magn. Reson 241 (2014) 3–17. [PubMed: 24656076]

[31]. Vold RL, and Vold RR, Deuterium Relaxation in Molecular Solids in: Warren W, (Ed.), Advances in Magnetic and Optical Resonance, Acadenic Press, San Diego, 1991, pp. 85–171.

[32]. Vold RR, Deuterium NMR studies of dynamics in solids and liquid crystals in: Tycko R, (Ed.), Nuclear Magnetic Resonance Probes of Molecular Dynamics, Kluwer academic Publishers, Dordrecht, 1994, pp. 27–112.

[33]. Perera SMDC, Xu X, Molugu TR, Struts AV, and Brown MF, Solid-State Deuterium NMR Spectroscopy of Rhodopsin in: Webb GA, (Ed.), Modern Magnetic Resonance, Springer International Publishing, Cham, 2018, pp. 1251–1270.

[34]. Ferreira HE, and Drobny GP, Biointerfaces 12 (2017) 02D418.

[35]. Ying WW, Irvine SE, Beekman RA, Siminovitch DJ, and Smith SO, J. Am. Chem. Soc 122 (2000) 11125–11128.

[36]. Molugu TR, Lee S, and Brown MF, Chem. Rev 117 (2017) 12087–12132. [PubMed: 28906107]

[37]. Hong M, Zhang Y, and Hu FH, Membrane Protein Structure and Dynamics from NMR Spectroscopy in: Johnson MA, and Martinez TJ, (Eds.), Annual Review of Physical Chemistry, Vol 63, 2012, pp. 1–24.

[38]. Au DF, Ostrovsky D, Fu R, and Vugmeyster L, J. Biol. Chem 294 (2019) 5840–5853. [PubMed: 30737281]

[39]. Meirovitch E, Liang Z, and Freed JH, J. Phy.s Chem .B 122 (2018) 4793–4801.

[40]. Vugmeyster L, Ostrovsky D, and Fu R, ChemPhysChem. 21 (2020) 220–231. [PubMed: 31805217]

[41]. Vugmeyster L, and Ostrovsky D, Chemphyschem. 20 (2019) 333–342. [PubMed: 30079456]

[42]. Vugmeyster L, Au DF, Ostrovsky D, and Fu R, ChemPhysChem. 20 (2019) 1680. [PubMed: 31087613]

[43]. Larsen FH, Jakobsen HJ, Ellis PD, and Nielsen NC, J. Phys. Chem. A 101 (1997) 8597–8606.

[44]. Vega AJ, J. Magn. Reson 96 (1992) 50–68.

[45]. Abragam A, Principles of Nuclear Magnetism, Clarendon Press, Oxford, 1961.

[46]. van der Maarel JRC, J. Chem. Phys 99 5646–5653.

[47]. Isotope labeling in Biomolecular NMR. in: Atreya HS, (Ed.), Isotope Labeling in Biomolecular NMR, 2012, pp. 1–219.

[48]. Beckmann PA, and Dybowski C, J. Magn. Reson 146 (2000) 379–380. [PubMed: 11001855]

[49]. Zhang D, Itin B, and McDermott AE, J. Magn. Reson 308 (2019) 106574. [PubMed: 31541931]

[50]. Vold RL, Hoatson GL, Vugmeyster L, Ostrovsky D, and De Castro PJ, Phys. Chem. Chem. Phys 11 (2009) 7008–7012. [PubMed: 19652835]

[51]. Ashbrook SE, and Wimperis S, J. Chem. Phy.s 120 (2004) 2719–31.

[52]. Larsen FH, Simulation of Molecular Motion of Quadrupolar Nuclei in Solid-State NMR Spectra, Annual Reports on Nmr Spectroscopy, Vol 71, 2010, pp. 103–137.

[53]. Vallurupalli P, Bouvignies G, and Kay LE, J. Am. Chem. Soc 134 (2012) 8148–61. [PubMed: 22554188]

[54]. Fawzi NL, Ying J, Ghirlando R, Torchia DA, and Clore GM, Nature 480 (2011) 268–72. [PubMed: 22037310]

[55]. Petkova AT, Leapman RD, Guo ZH, Yau WM, Mattson MP, and Tycko R, Science 307 (2005) 262–265. [PubMed: 15653506]

[56]. Brannstrom K, Ohman A, Nilsson L, Pihl M, Sandblad L, and Olofsson A, J. Am. Chem. Soc 136 (2014) 10956–64. [PubMed: 25014209]

[57]. Scheidt HA, Morgado I, Rothemund S, and Huster D, J. Biol. Chem 287 (2012) 2017–2021. [PubMed: 22130659]

[58]. Petkova AT, Yau WM, and Tycko R, Biochemistry 45 (2006) 498–512. [PubMed: 16401079]

[59]. Bertini I, Gonnelli L, Luchinat C, Mao J, and Nesi A, J. Am. Chem. Soc. 133 (2011) 16013–16022. [PubMed: 21882806]

[60]. Olofsson A, Sauer-Eriksson AE, and Ohman A, J. Biol. Chem 281 (2006) 477–483. [PubMed: 16215229]

[61]. Brown MJ, Vold RL, and Hoatson GL, Solid State Nucl. Magn. Reson 6 (1996) 167–85. [PubMed: 8784956]

[62]. Relaxation of Quadrupolar Nuclei Measured via Multiple-Quantum Filtration, eMagRes.(2007) doi: 10.1002/9780470034590.emrstm0462

[63]. Duer MJ, Solid-State NMR Spectroscopy, Blackwell Publishing Ltd, Oxford, 2004.

[64]. Kristensen JH, Hoatson GL, and Vold RL, J. Chem. Phys 110 (1999) 4533–4553.

[65]. Cutajar M, Ashbrook SE, and Wimperis S, Chem. Phys. Lett 423 (2006) 276–281.

[66]. Duer MJ, and Stourton C, J. Magn. Reson 129 (1997) 44–52. [PubMed: 9405215]

[67]. Hoffmann A, and Schnell I, Chemphyschem. 5 (2004) 966–974. [PubMed: 15298382]

[68]. Huang YY, Vold RL, and Hoatson GL, J. Chem. Phys 124 (2006).

[69]. Vugmeyster L, Ostrovsky D, Penland K, Hoatson GL, and Vold RL, J. Phys. Chem. B 117 (2013) 1051–1061. [PubMed: 23301823]

[70]. Sun C, Mitchell O, Huang JX, and Boutis GS, J. Phys. Chem. B 115 (2011) 13935–13942. [PubMed: 22017547]

[71]. Vugmeyster L, and Ostrovsky D, Magn. Reson. Chem 10.1002/mrc.5114 (2020).

[72]. Wimperis S, J. Magn. Reson 86 (1990) 46–59.

[73]. Hoatson GL, J. Magn. Reson 94 (1991) 152–159.

[74]. Grey C, Veeman WS, and Vega AJ, J. Chem. Phys 98 (1993) 7711–7724.

[75]. Akbey U, Nieuwkoop AJ, Wegner S, Voreck A, Kunert B, Bandara P, Engelke F, Nielsen NC, and Oschkinat H, Angew. Chem 53 (2014) 2438–42. [PubMed: 24474388]

[76]. Jain SK, Nielsen AB, Hiller M, Handel L, Ernst M, Oschkinat H, Akbey U, and Nielsen NC, Phys. Chem. Chem. Phys 16 (2014) 2827–2830. [PubMed: 24418905]

[77]. Bjerring M, Paaske B, Oschkinat H, Akbey Ü, and Nielsen NC, J. Magn. Reson 214 (2012) 324–328. [PubMed: 22130517]

[78]. Matlahov I, and van der Wel PCA, Methods 148 (2018) 123–135. [PubMed: 29702226]

[79]. Asami S, and Reif B, Acc. Chem. Res 46 (2013) 2089–2097. [PubMed: 23745638]

- We review ^{2}H static ssNMR methods for studies of slow motions in proteins.
- Main methods include: rotating frame relaxation dispersion,
- quadrupolar Carr–Purcell–Meiboom–Gill relaxation dispersion,
- quadrupolar chemical exchange saturation transfer.
- Applications are chosen from amyloid-β fibrils.

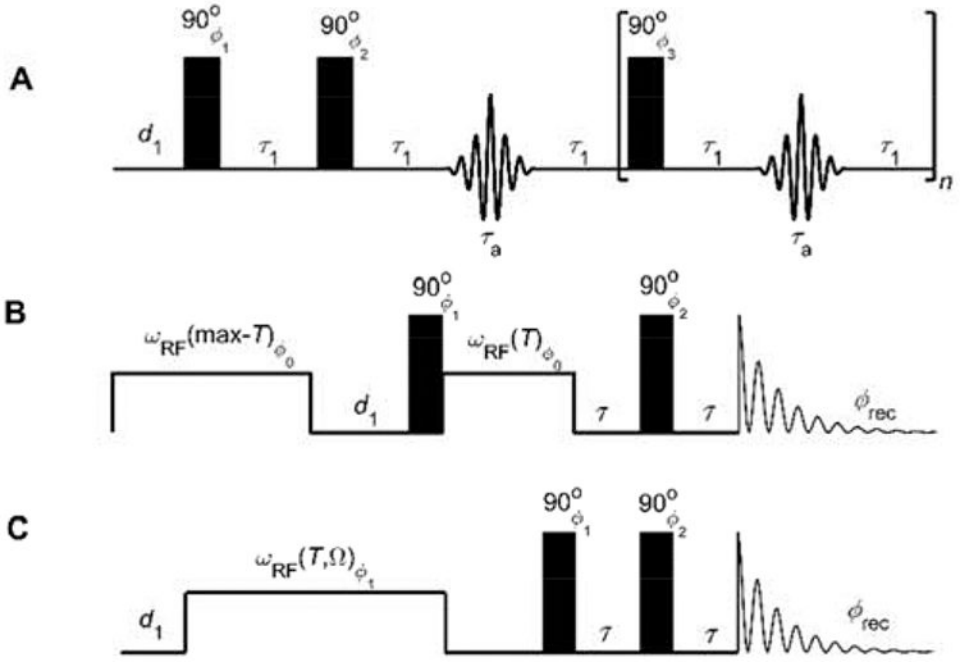

Figure 1.

^{2}H static/solid-state NMR pulse sequences [40,41,42] A) Time-domain QCPMG: The full quadrupolar echo acquisition period (τ_a) is followed by the train of echo units (in square brackets). d_1 is the inter-scan delay and τ_1 is the pulse ringing delay $\tau_{QCPMG} = \tau_a + 2\tau_1 + 90°/2$. The following 16-step phase cycle is used: ϕ_1=*x,y,−x,−y*; ϕ_2= *y,x,y,x,−y,−x,−y,−x*; ϕ_3= *y,x,y,x,−y,−x,−y,−x, −y,−x,−y,−x, y,x,y,x*; ϕ_{rec}= *−x,−y,x,y.* Modified from Larsen et al. [43] B) $R_{1\rho}$: the ω_{RF}(max-*T*) block is designed to provide heat compensation; the preparation 90° pulse produces transverse magnetization and is followed by a variable spin-lock delay ω_{RF} (*T*).[41] Detection is preceded by the quadrupolar echo. The phase cycle corresponds to ϕ_0=*x*; ϕ_1= *−y,y*; ϕ_2= *−x,x*; ϕ_{rec} = *−y,y*. C) Q-CEST: The small amplitude RF saturation pulse ω_{RF} (*T*,Ω) acting on the longitudinal coherence is followed by the quadrupolar echo for detection. [40] The phase cycle is ϕ_1=*x,−y, −x, y, x,−y, −x, y*; ϕ_2=*−y, −x, y, x, y, x, −y, −x*; ϕ_{rec}=*−y, −x, y, x, −y, −x, y, x.*

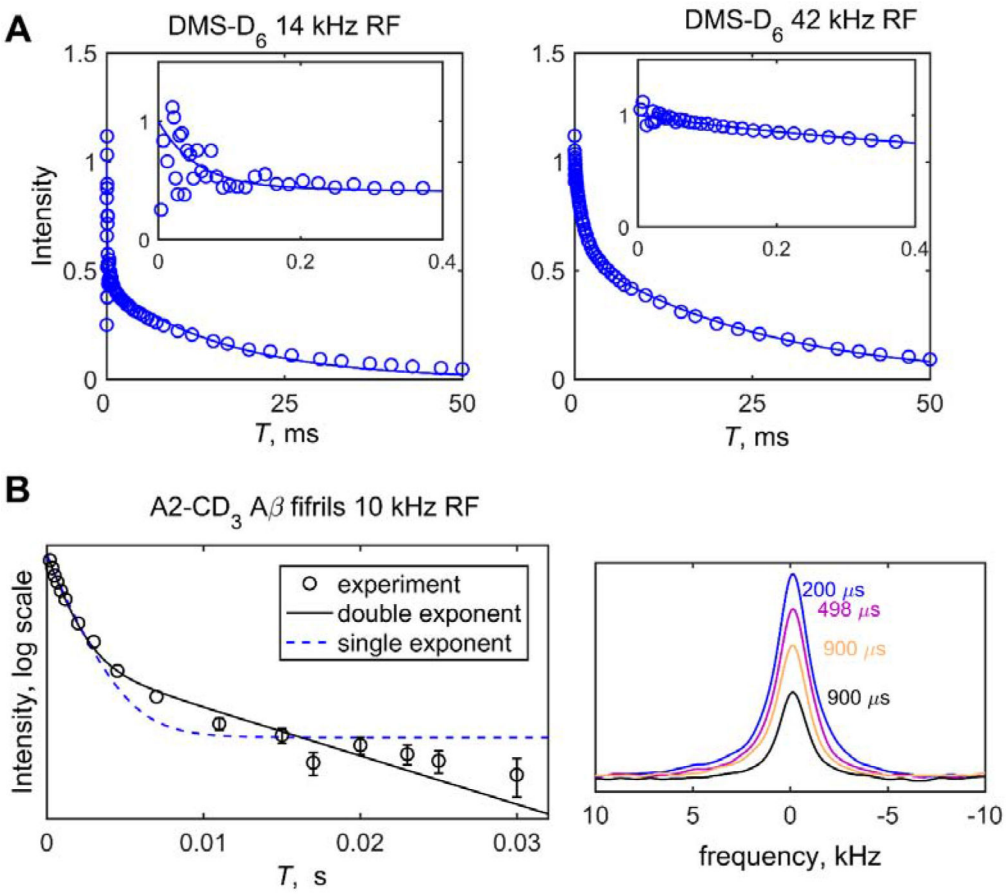

Figure 2.

Examples of the experimental decay curves for the $R_{1\rho}$ experiment obtained with the pulse sequence shown in Figure 1B. A) Dimethyl-sulfone-D_6 at two values of the spin-lock field for the major singularities (horns) positions of the powder pattern at 73°C and 14.1 T field strength. The solid lines correspond to the two-exponential fit. The inserts highlight the initial decay region.[41] B) Example for the A2-CD_3 site of the $A\beta_{1\text{-}40}$ fibrils in the 3-fold symmetric polymorph for a 10 kHz RF field strength.[38] Integrals of the central peak intensities (circles) versus time shown on a semi-log scale. Integration was taken over the half-height spectral regions. The fits to the single-exponential function are shown by the blue dotted lines, while the double-exponential fits are shown as the black lines. Examples of the partially relaxed line shapes are displayed in the right panel, highlighting a pronounced spectral narrowing. Data were acquired at 37°C with the static magnetic field strength of 14.1 T.

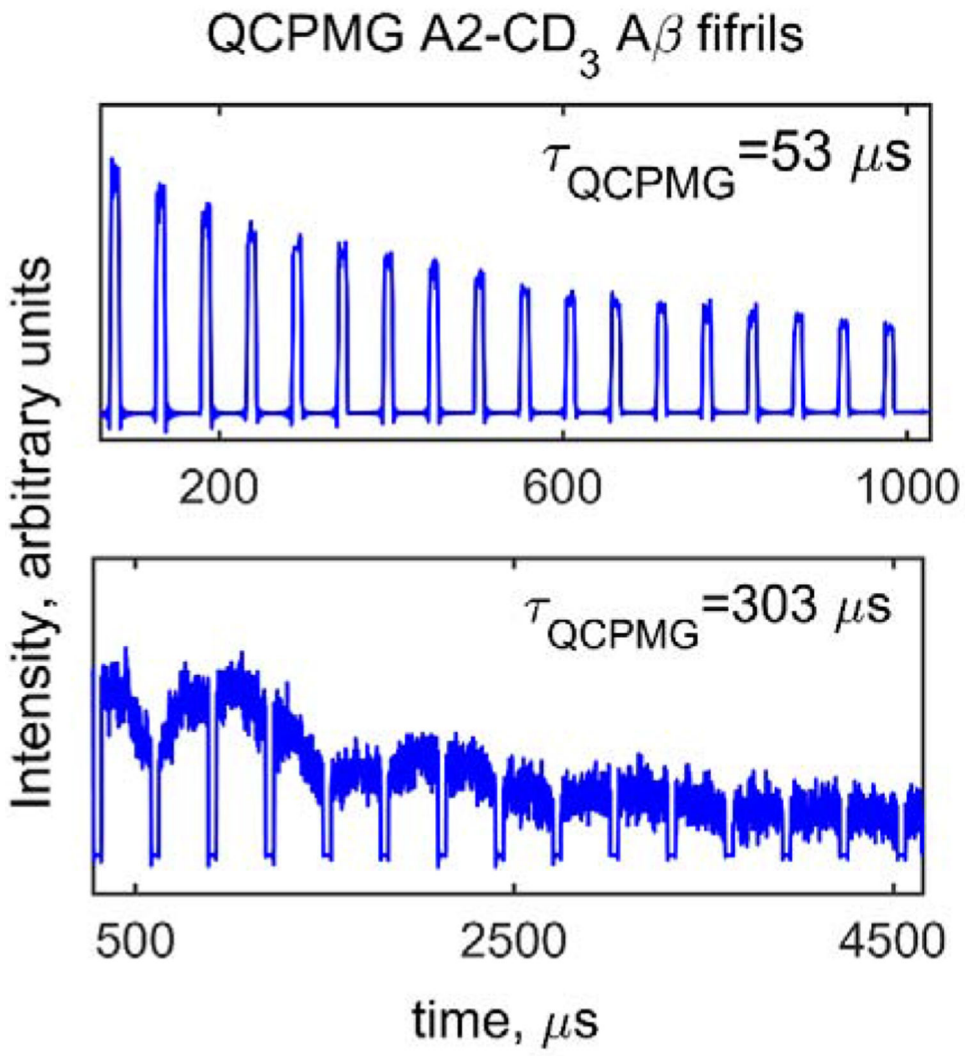

Figure 3.

^{2}H QCPMG free induction decays obtain with pulse sequence of Figure 1A, shown from the first echo in the repeated echo unit (designated by the square brackets in the pulse sequence) for two values of τ_{QCPMG}. Acquired at 14.1 T and 37°C for the A2-CD_3 site of the hydrated $A\beta_{1\text{-}40}$ fibrils in the 3-fold symmetric polymorph.[42]

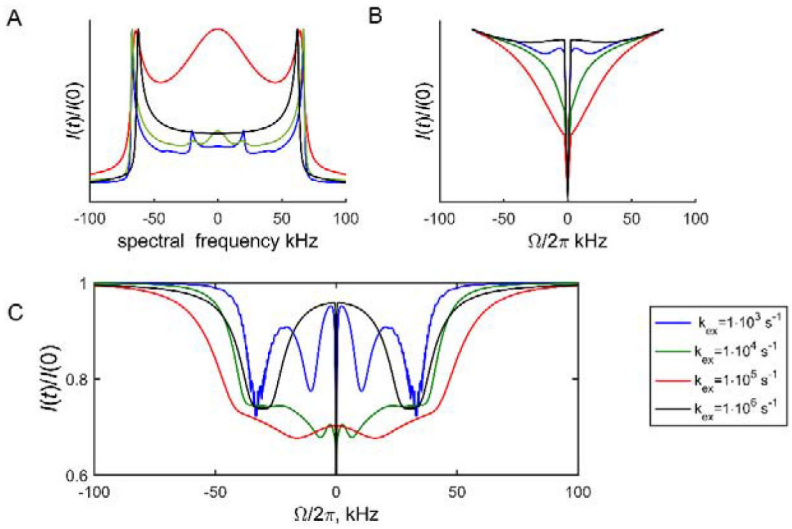

Figure 4.

Simulated effects of the 2-site conformational exchange with $C_{q,1}$=55 kHz, $C_{q,2}$=180 kHz, $\eta_1=\eta_2=0$, p_1=10%, and different values of k_{ex}. A) ^{2}H powder pattern line shapes. B) $I(t)/I(0)$ for powder averages versus the off-resonance offset $\Omega/2\pi$ for the saturation time of 100 ms and $\omega_{RF}/2\pi$ = 2 kHz. C) $I(t)/I(0)$ versus the offset $\Omega/2\pi$ for a selected crystallite orientation with $\omega_{Q,1}/2\pi$ =33.1 kHz and $\omega_{Q,2}/2\pi$ =10.1 kHz.[40]

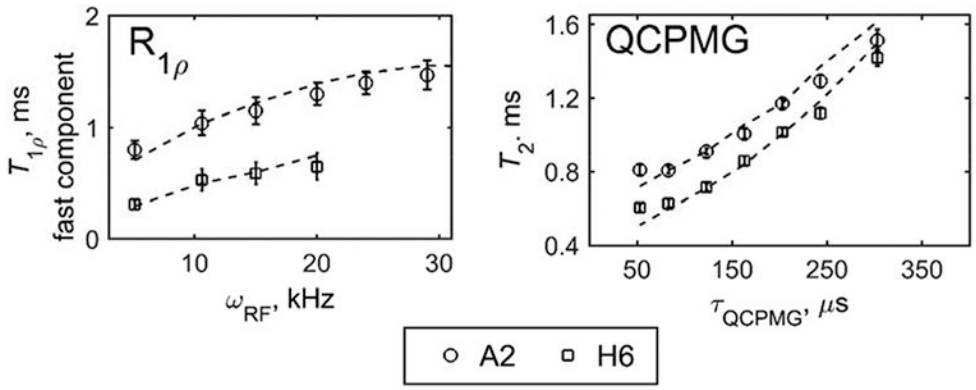

Figure 5.

Selected experimental ^{2}H relaxation dispersion profiles for the N-terminal domain methyl group sites of the hydrated A$\beta_{1\text{-}40}$ fibrils at 37°C and 14.1 T.[38,42] $R_{1\rho}$ experiment: the fast relaxing component of the double-exponential fits of the magnetization decay curves (Figure 2) versus the spin-lock field strength. QCPMG: transverse relaxation time T_2 versus τ_{QCPMG}, resulting from the mono-exponential fits of the magnetization decay curves (Figure 3). The lines represent the fits to the model shown in Figure 6.

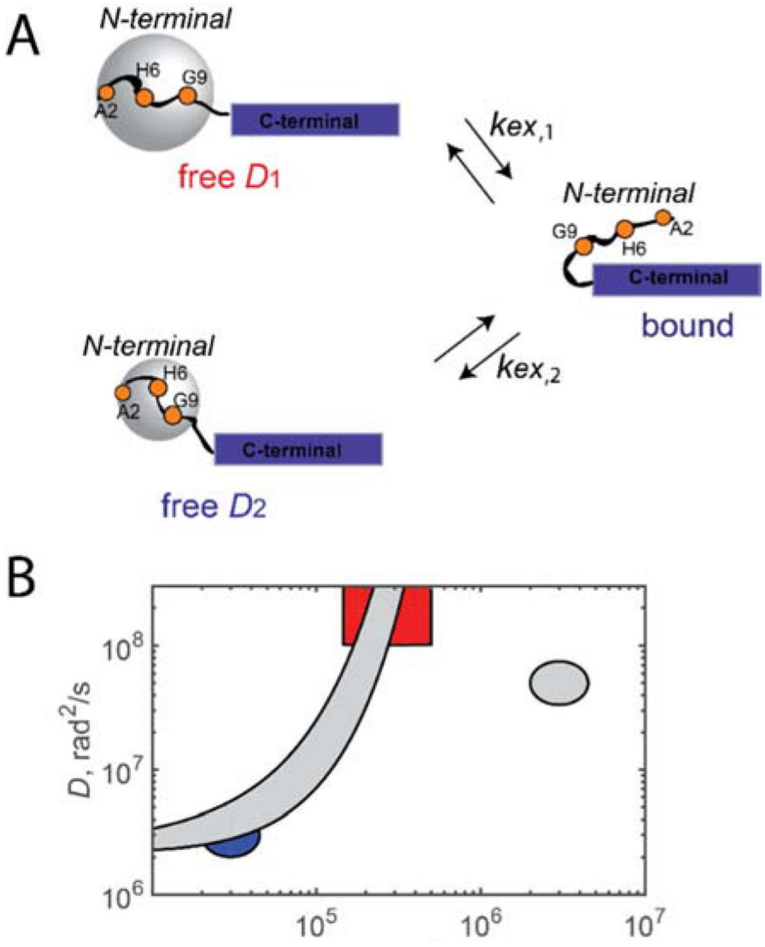

Figure 6.

A) Cartoon representation of the motional model (three states) for the disordered N-terminal domain of the hydrated $A\beta_{1\text{-}40}$ fibrils.[42] The N-terminal domain is represented by the curved line, while the structured C-terminal domain is shown as the blue rectangle. The bound state arises due to transient interactions between the two domains. In the two free states, the N-terminal domain is subject to the isotropic diffusion with the diffusion coefficients D_1 and D_2, $D_1 \gg D_2$, shown as the gray spheres, while in the bound state, interactions freeze this mode. The chemical exchange rate constants corresponding to these interactions are $k_{ex,1}$ and $k_{ex,2}$, respectively. The model also includes the relative populations of all the states. B) A two-dimensional (D versus k_{ex}) schematic representation of the sensitivity of the probed time scales for the QCPMG (red), $R_{1\rho}$ (blue), and Q-CEST (gray) experiments for the A2-CD_3 site in the $A\beta_{1\text{-}40}$ fibrils obtained from the χ^2 values of the corresponding fits.

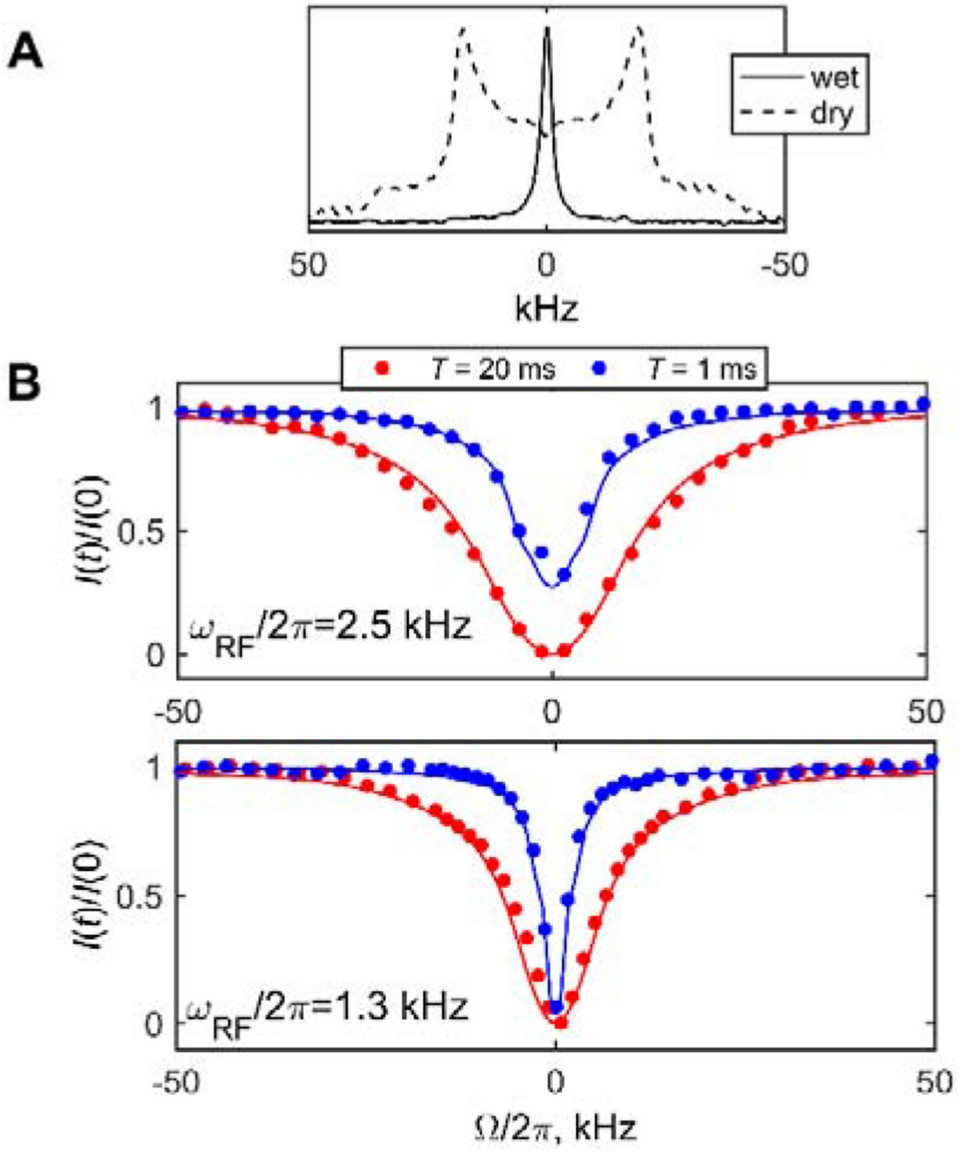

Figure 7.

Experimental results for the A2-CD_3 site in the hydrated $A\beta_{1\text{-}40}$ fibrils recorded at 37°C and 14.1 T. A) ^2H static/solid-state NMR line shapes for the dry (dotted line) and hydrated (solid line) states.[38] B) Experimental (circles) and simulated (lines) Q-CEST profiles. $I(t)/I(0)$ integrated over the entire spectrum versus $\Omega/2\pi$ for saturation times of 20 ms (red) and 1 ms (blue) and $\omega_{RF}/2\pi$ of 1.3 and 2.5 kHz, as indicated on the panels. Simulations were performed according to the model in Figure 6A, as described in the text. Reprinted from [40] with a permission from the publisher.